Geothermics 84 (2020) 101740

Contents lists available at ScienceDirect

Geothermics

journal homepage: www.elsevier.com/locate/geothermics

Spatiotemporal variations of in situ V_p/V_s ratio within the Salton Sea Geothermal Field, southern California

Guoqing Lin

Department of Marine Geosciences, Rosenstiel School of Marine and Atmospheric Science, University of Miami, Miami, FL 33149, USA

ARTICLE INFO

Keywords:
Salton Sea Geothermal Field
In situ V_p/V_s ratio
Porosity
Heat flow

ABSTRACT

The Salton Sea Geothermal Field is located on the southeastern shore of Salton Sea and has been facilitated with many geothermal units in the past few decades. In this study, I investigate possible effects of the long-term production process on seismic parameters by using a high-resolution approach to estimate the near-source compressional- to shear-wave velocity ratios (V_p/V_s). I apply this method to similar earthquake clusters based on waveform cross-correlation data and obtain robust results for six event clusters in the study area. The resulting in situ V_p/V_s ratios vary from 1.510 to 1.811 with the calculated uncertainties below 0.02. I examine possible relations between these V_p/V_s ratios and other types of data. The observed spatial correlation with the heat flow and temporal correlation with well production data indicate that the near-source V_p/V_s ratios strongly depend on the subsurface natural properties, but are influenced by the amount of extraction and injection volume throughout the operational period. This study suggests that the in situ estimation method can be used to detect changes in near-source V_p/V_s ratios caused by exploitation of geothermal areas and is a potentially valuable tool for geothermal resource monitoring.

1. Introduction

The Salton Trough region in the southeastern portion of southern California is geologically active and contains abundant geothermal resources. The largest development is located on the southeast shore of Salton Sea and is referred to as the Salton Sea Geothermal Field (Fig. 1). The operation in the Salton Sea Geothermal Field (SSGF) commenced in the early 1980s with a total potential resource of 2000 megawatts electric. This area is characterized by the extensional tectonic regime with high seismicity and strong subsidence. Numerous studies have been carried out to investigate the effects of the long-term production process on the local seismic activity and stress field. Chen and Shearer (2011) observed lower stress drops within the geothermal field and suggested a dependence on distance from injection well locations. It has been shown that the seismicity rate in the SSGF is correlated with the production of geothermal energy (Brodsky and Lajoie, 2013; Ellsworth, 2013; Llenos and Michael, 2016). It was suggested that the most likely mechanism for the high subsidence rates at the SSGF is the fluid-mass loss associated with the geothermal operations, although the effects of natural sources cannot be precluded (Barbour et al., 2016a, 2016b). It was claimed that the seismicity within the SSGF does not respond to remote triggering of large distant earthquakes as actively as the nearby tectonic earthquakes (Zhang et al., 2017). A long-term velocity increase was detected in the SSGF and was interpreted most likely due to poroelastic contraction caused by the geothermal production (Taira et al., 2018). Relatively higher *b*-values and large number of smaller earthquakes were observed within the geothermal field than the outside area (Cheng and Chen, 2018). All these studies imply that the anthropogenic activity has altered the local stress state inside the geothermal field. However, given the coarse production data (monthly rates) available to the public, it remains difficult to find unambiguous temporal correlations between the production rates/volumes and seismic parameters.

The ratio of compressional- to shear-wave velocity (V_p/V_s) is directly related to Poisson's ratio and is sometimes more important than V_p and V_s separately in characterizing crack and fluid properties and analyzing the effect of pore fluid pressure (Takei, 2002). Changes in V_p/V_s ratios can be used to track presence and movement of volatiles and estimate variations in fracturing and fluid content. V_p/V_s ratio has been widely investigated in geothermal fields and used to constrain the composition of rocks, the presence of cracks, the degree of pore fluid saturation, and other properties. In the Long Valley geothermal field, high V_p (Seccia et al., 2011) and low V_p/V_s anomalies (Lin, 2015) are observed at shallow depths near the Long Valley Exploratory Well. In the Geysers Geothermal Field, dominating low V_p/V_s ratios ($\sim$1.58) are a common feature of the existing V_p/V_s models corresponding to the exploited section of the geothermal reservoir (Julian et al., 1996, e.g.,]

E-mail address: glin@rsmas.miami.edu.

https://doi.org/10.1016/j.geothermics.2019.101740
Received 19 April 2019; Received in revised form 24 July 2019; Accepted 26 September 2019
Available online 07 October 2019

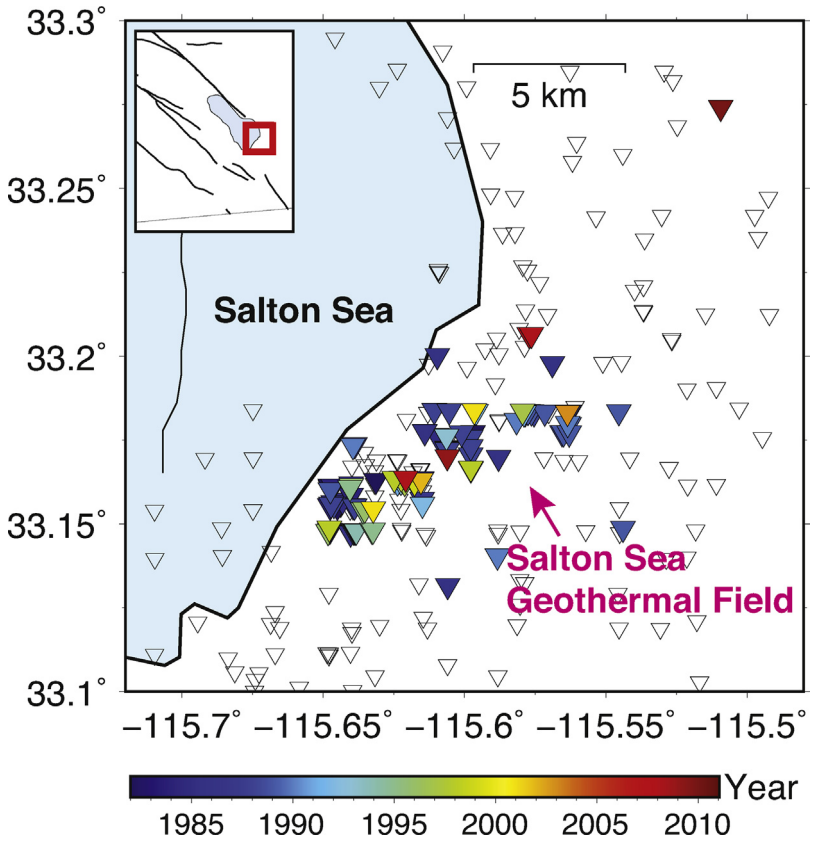

Fig. 1. Locations of the geothermal wells in the study area. Currently active wells are colored by the year of drilling. Open triangles represent abandoned or idle wells. The red box in the inset map shows the location of the study area in southern California.

[; Foulger et al., 1997; Kirkpatrick et al., 1997; Gritto et al., 2013; Gritto and Jarpe, 2014; Lin and Wu, 2017), which is usually explained by low pore pressure and dry conditions at depth. In the Coso geothermal field, low V_p/V_s features within the production area are observed by previous studies (Walck, 1988; Lees and Wu, 2000; Zhang and Lin, 2014) and are interpreted to be affected by vapor. Lin (2013) presented that one of the most significant features in the V_p/V_s model for Salton Trough is the predominantly low V_p/V_s values below 2 km depth and the lowest V_p/V_s ratios occur in the Salton Sea area.

The majority of the above studies are based on seismic tomography, one of the most commonly applied techniques for mapping V_p/V_s ratios. However, detection of spatiotemporal variations in tomographic V_p/V_s ratios can be difficult to achieve because of the non-uniqueness of the problem and the difficulties of obtaining reliable V_p/V_s models, limited by data availability, data quality, ray coverage, and grid spacing deployed in inversions. In this study, I apply a high-resolution estimation method using waveform cross-correlation data to calculate in situ V_p/V_s ratios in the near-source regions of the SSGF and to investigate any spatiotemporal variations in V_p/V_s ratio that may be associated with the local anthropogenic activity.

2. Data

In this study, I take advantage of the available data and model for Salton Trough by Lin (2013), based on the seismic data from 1981 to September 2010 originated from the Southern California Earthquake Data Center (SCEDC, 2013). The three-dimensional (3-D) seismic velocity model, initiated from the 3-D regional-scale model for California by Lin et al. (2010), is more consistent with the refraction studies and well correlates with geological features at shallow depths. The high-precision earthquake relocation catalog (Fig. 2) has improved accuracies in both absolute and relative locations based on the ray-tracing

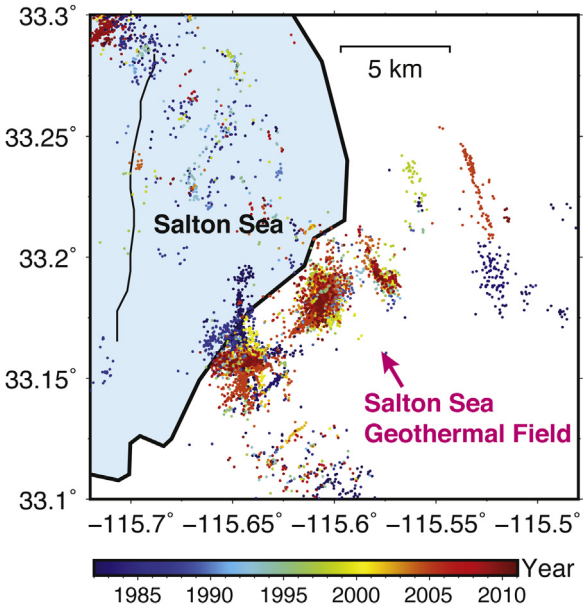

Fig. 2. Map view of the waveform cross-correlation relocations from 1982 to September 2010 near the Salton Sea Geothermal Field (Lin, 2013), colored by the year of event occurrence.

through the 3-D velocity model and waveform cross-correlation data. The 231 million *P*- and *S*-wave differential times for 7.5 million event pairs and the corresponding correlation coefficients are also available. All the injection and extraction data used in this study are downloaded from the Division of Oil, Gas, and Geothermal Resources (DOGGR, last accessed in August 2018).

3. Methodology

The high-resolution V_p/V_s ratio estimation method applied in this study is developed and described by Lin and Shearer (2007). It uses differential times from waveform cross-correlation to study spatial and temporal variations of near-source V_p/V_s ratios in different tectonic regions. The basic idea of this method is as follows. For a compact cluster of events, the waveforms for each pair of events observed at the same station will be similar enough so that the cross-correlation can be computed. This method assumes that the scale length of changes in the V_p/V_s ratio is greater than the size of the similar event clusters so that the V_p/V_s ratio can be treated as a constant within the event cluster. This makes it possible to fit all the points of the demeaned differential *P*- and *S*-arrival times simultaneously for the best-fitting V_p/V_s ratio for the entire cluster. A hybrid L_1–L_2 fitting method is described in Lin and Shearer (2007), which is more robust to outliers in the observations than the traditional least squares fitting.

The most accurate V_p/V_s results for real data can be obtained for clusters with a three-dimensional distribution of events (Lin and Shearer, 2007). In order to estimate the spatial distribution of events in each cluster, I use the method of principal component analysis [e.g., Kirschvink, 1980] to compute eigenvalues for the covariance matrix of the earthquake locations for all similar event clusters. Clusters are considered to have nearly spherical distribution if $\lambda_1/\lambda_3 \leq K$, (where eigenvalues $\lambda_1 \geq \lambda_2 \geq \lambda_3$, K is a constant) (Michelini and Bolt, 1986; Shearer et al., 2003; Lin and Shearer, 2009; Lin and Thurber, 2012; Lin et al., 2015). Standard errors in the estimated V_p/V_s ratios are calculated by applying a bootstrap approach (Efron and Gong, 1983; Efron and Tibshirani, 1991), in which each pair of suitable differential *P* and *S* times in the same cluster may be sampled multiple times or not sampled at all. This process is repeated for many subsamples for each cluster and the standard deviation of these subsamples is used as the standard error of the V_p/V_s ratio.

This method for estimating V_p/V_s ratios offers several useful advantages. First, it provides highly precise results because cross-correlation can measure differential times to within a few milliseconds and can achieve a precision of 0.001 in estimated V_p/V_s ratio. This method is simple to implement and fast to execute since it uses a robust least-squares to fit the differential times. Another advantage of this method is that it is straightforward to study the spatial and temporal variations of V_p/V_s ratios by simply selecting a subset of events by space and/or time.

4. Application to the SSGF

I apply the V_p/V_s ratio estimation method to the similar earthquake clusters based on waveform cross-correlation by Lin (2013). Each cluster is composed of event pairs with correlation coefficients above a given threshold and is identified starting from the highest correlated event pair. The specifics of the cluster analysis method are detailed in Shearer et al. (2005). During the V_p/V_s ratio estimation, I use the waveform data from the entire southern California seismic network and constrain *P* measurements from the vertical component and favor *S* measurements from the horizontal components, and then select the one with the highest correlation coefficient. I require each event pair have at least 8 individual differential times with correlation coefficients of 0.65 or greater and only differential times with a waveform correlation coefficient of 0.6 or greater are used in the calculation. Because the waveform data from the SCEDC and the corresponding relocations are only available for events since 1981 (Lin, 2013) and the focus of this paper is on the effect of the geothermal operation (commenced in 1982), only seismic data from 1981 to September 2010 near the SSGF injection/production wells are used in the following analyses (Fig. 2). Furthermore, I select the clusters with $\lambda_1/\lambda_3 \leq 10$ and the estimated standard errors in V_p/V_s less than 0.03 near the SSGF for further discussion.

The resulting V_p/V_s ratio for each cluster represents the average value in both space and time because of the spatial extent and time span of all the events in the cluster. In order to compare with the injection and extraction data, it would be ideal to explore temporal variations in V_p/V_s ratio by separating earthquakes into different time periods (e.g., monthly or yearly) before performing similar event cluster analysis. Unfortunately, there are no sufficient data samples every year in the study area to carry out this investigation. Instead, I assign the V_p/V_s ratio of each cluster to all its events and group all the events in all the clusters by the year of occurrence. I then calculate the average V_p/V_s ratio each year and take the time series as the temporal variation of the near-source V_p/V_s ratio.

5. Results

After the application of the in situ method, there are 6 similar event clusters within the SSGF that satisfy the selection criteria, consisting of 5,444 events. Both absolute and relative location uncertainties are available for events in these clusters (Lin, 2013). The median absolute location uncertainty is 91 m in horizontal and 128 m in vertical, estimated during the simultaneous tomography and location inversion. The median relative location uncertainty is 11 m for the horizontal and 18 m for the vertical, estimated by applying a bootstrap approach during the waveform cross-correlation relocation. The magnitudes of these events span from 0 to 5.1. The average correlation coefficients of both *P*- and *S*-waves are above 0.76 for all the clusters with the standard deviations of ~0.10. These clusters are centered between 2.5 and 4.6 km depths and the average interevent distances are all around 2 km. The estimated in situ V_p/V_s ratios for the 6 clusters vary from 1.510 to 1.811. More characteristics of these earthquake clusters are summarized in Table 1.

In Fig. 3, I show distribution of the seismicity in the 6 clusters colored by their corresponding in situ V_p/V_s ratio. In the map view (Fig. 3a), the V_p/V_s ratio in cluster 1, which is located in the most southwestern section, is 1.686, slightly lower than a regular V_p/V_s value (~1.73). Along profile A-A' to the northeast direction, the V_p/V_s ratios start to decrease to about 1.63 and then below 1.6. Cluster 6, positioned in the area where there are no currently active geothermal wells, has the highest V_p/V_s value of 1.811. It is also worthwhile pointing out that the V_p/V_s ratios in the two clusters outside of the pink box (i.e. southeast of the SSGF) are at the regular V_p/V_s values of 1.73. The cross-section in Fig. 3b shows that the clusters with lower V_p/V_s ratios (1.51-1.63) are located in the middle of the profile and have relatively shallower centers (above 3 km depth). The two clusters with slightly higher or normal V_p/V_s ratios are both centered below 4 km depth (also seen in Table 1).

6. Discussion

In this section, I evaluate the robustness of the results and investigate possible associations of V_p/V_s ratio with various parameters.

Table 1
Characteristics of the 6 earthquake clusters used in the analyses. λ_1 and λ_3 are eigenvalues for the covariance matrix of the earthquake locations for each cluster. The distances in the rows 7 and 8 are the interevent distance within each cluster. Rows 9 and 10 are the average correlation coefficients of P- and S-waves used in the V_p/V_s estimation for each cluster.

Cluster Index	1	2	3	4	5	6
No. of events	2,242	2,548	30	469	50	105
In Situ V_p/V_s	1.686	1.565	1.630	1.510	1.521	1.811
Uncertainty	0.005	0.005	0.019	0.011	0.016	0.008
λ_1/λ_3	4.6	3.4	5.0	3.7	3.0	3.6
Depth (km)	4.57	3.11	2.46	2.65	2.88	4.23
Avg-distance (km)	2.74	1.81	1.93	1.56	1.93	2.23
Max-distance (km)	16.51	9.53	4.56	8.82	6.87	7.35
Avg-P-Coef	0.78	0.76	0.81	0.78	0.76	0.77
Avg-S-Coef	0.76	0.76	0.87	0.78	0.79	0.77

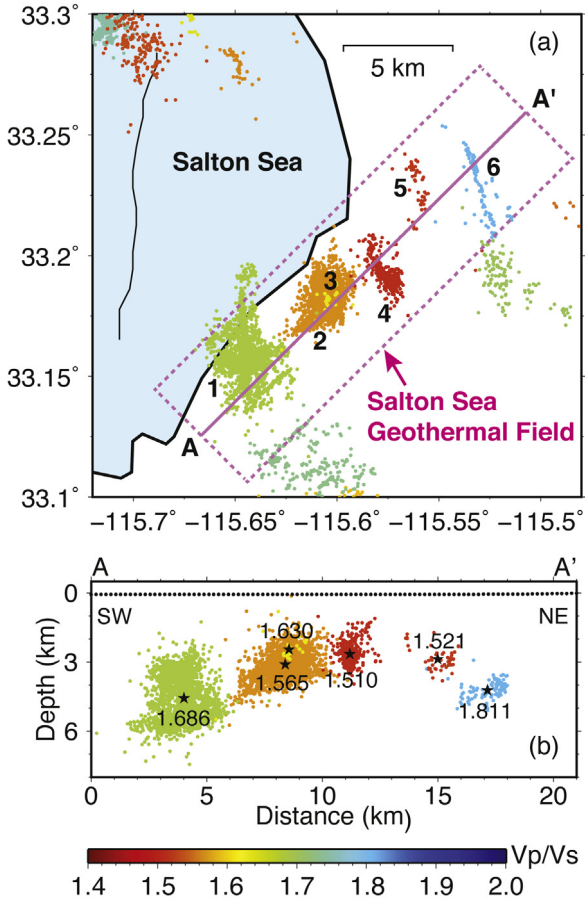

Fig. 3. (a) Map view of events in the similar earthquake clusters, colored by the in-situ V_p/V_s ratio for each cluster. The number next to each cluster is the cluster index in Table 1. The pink straight line and dotted box are the profile and boundary for the cross-sections in (b). (b) Depth distribution of seismicity in each cluster enclosed by the pink box along profile A-A' in (a). Events in each cluster are centered at the black star and are colored by the corresponding in situ V_p/V_s ratio (number next to each star). Zero depth refers to mean sea level (~60 m below ground surface). The black dots at the top of the cross section show the local topography.

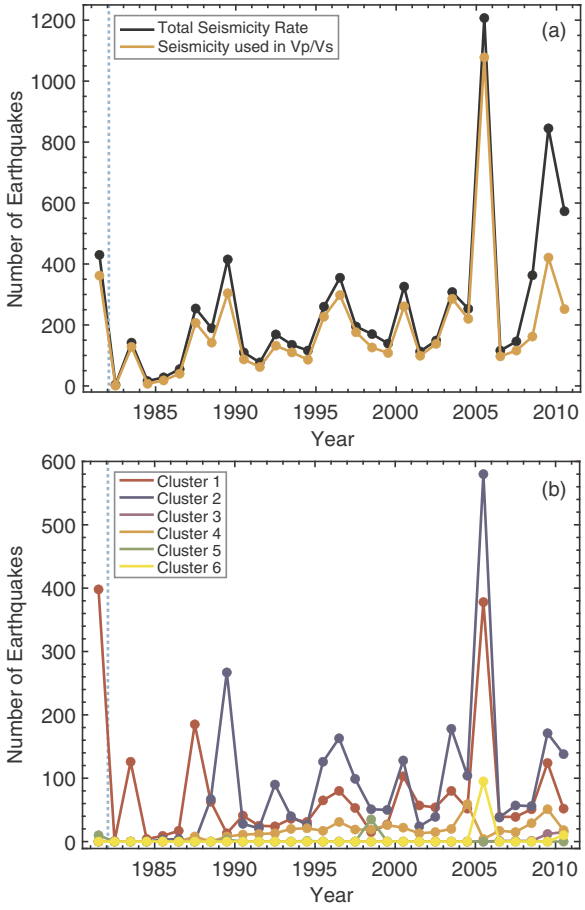

Fig. 4. (a) Number of earthquakes per year within the dotted box in Fig. 3(a). Black curve indicates all the relocated seismicity by Lin (2013). Orange one shows the seismicity used in the V_p/V_s ratio estimation. (b) Number of earthquakes per year in each cluster. Values in year 1981 are also included as a background reference.

6.1. Seismicity rate

In order to examine whether the data used in the V_p/V_s estimation are biased by any special features, I plot the yearly rate of all the seismicity and the number of earthquakes used in the V_p/V_s estimation within the pink box in Fig. 3a. In the overall seismicity rate (black curve in Fig. 4a), over 400 events took place in 1981, due to a seismic swarm (Lohman and McGuire, 2007). There is an abrupt decrease in 1982 when the geothermal activity commenced. The seismic activity remained quite low in the first few years after that, and then was relatively stable with about 100–300 events per year. The only two anomalies are in 2005 and 2009, when the seismic activity was dominated by local swarms. The rate of earthquakes used for V_p/V_s calculation (orange curve in Fig. 4a) shows the same pattern as for the entire seismicity but has slightly smaller numbers, indicating that the data used in the estimation are representative and cover the entire time period of the data set. The biggest discrepancy between the two rates occurs in 2009. The events that are not used in the V_p/V_s estimation are sparsely distributed around the earthquake clusters 1–4 and do not fall into similar event clusters based on the clustering criteria used in Lin (2013). This means that the data used in the V_p/V_s estimation are not spatially biased either. The annual seismicity rates for each similar earthquake cluster are also plotted in Fig. 4b. The three largest clusters (clusters 1, 2, and 4) comprise events throughout all the years in the study period. Clusters 3 and 6 are composed of events between 2005 and 2010, dominated by the two seismic swarms. Cluster 5 only includes events before 1999.

6.2. Tomographic model

In order to compare the in situ V_p/V_s ratios with the tomography model, I plot map views and cross-sections of the 3-D V_p and V_p/V_s models from Lin (2013) (Fig. 5). The average depth of the earthquakes in Fig. 3b is 3.7 km, therefore the velocity models are plotted at 4 km depth layers in the map views. In the cross-sections, I interpolate the tomographic model for the corresponding V_p or V_p/V_s value at each earthquake location. I then calculate the average velocity value from all the events in each cluster and color these earthquakes by the cluster-average velocity, similar to Fig. 3b. The tomographic V_p model (Fig. 5a and b) weakly correlates with the in situ V_p/V_s values, showing low velocity values in the middle section of the profile. Different from the in situ results, the map view of the tomographic V_p/V_s (Fig. 5c) is relatively uniform within the pink box, with a low anomaly at the edge of the SSGF. The cross-section comparison between Fig. 3b and 5 d illustrates similar patterns with lower values in the middle of the profile and higher ratios at the ends, despite the different absolute V_p/V_s values.

These comparisons suggest that the high-resolution V_p/V_s ratio estimation method may provide fine-scale velocity structure that cannot be easily resolved by tomographic methods, which are often restricted

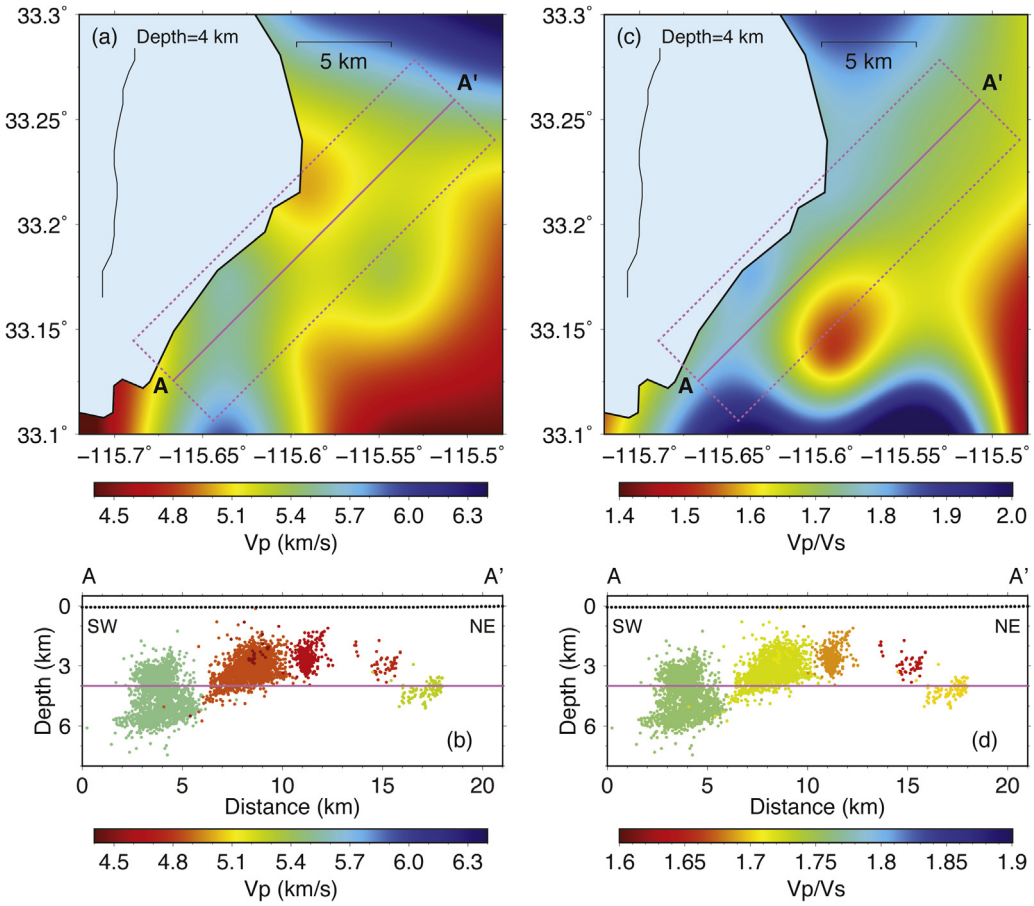

Fig. 5. (a, c) Map view of the tomographic V_p and V_p/V_s model at 4 km depth (relative to mean sea level), respectively. (b, d) Cross-section of seismicity in the similar earthquake clusters (same as those in Fig. 3b) colored by the average tomographic V_p and V_p/V_s values for each cluster, respectively. Note that different color scales are used for the V_p/V_s map view and cross-section. The pink horizontal lines mark 4 km depth where the map views are plotted.

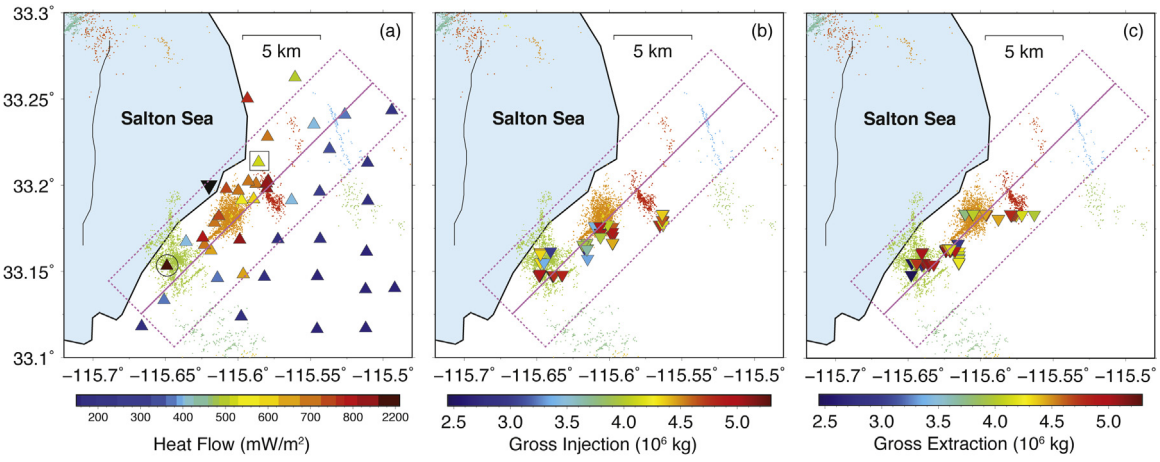

Fig. 6. (a) Site heat flow values downloaded from the SMU Geothermal Lab. The circled triangle has the highest heat flow value of 2200 mW/m^2. The boxed triangle has a known well depth of 3.22 km. The inverted black triangle next to the coastline of Salton Sea shows the location of Salton Buttes. (b) Gross injections from 1982 to 2010 at each well location in $\log_{10}$ scale. (c) Gross extractions from 1982 to 2010 at each well location in $\log_{10}$ scale. The dotted box and profile in each sub-figure are the same as those in Fig. 3(a) and are included as a location reference.

by data quality, ray coverage, and inversion grid size (5 km in this case), and may be affected by node positions. McGuire et al. (2015) showed that the V_p structure within the SSGF is higher than the outside of the field, also seen in the model by Lin (2013), and attributed it to the denser, more feldspathic rock altered from the shallow sandstone sedimentary layers. The correlation with the tomographic V_p model implies that the in situ V_p/V_s ratios depend on rock composition and mineralogy.

6.3. Heat flow

The broad Salton Trough region has been known for high heat flow (~140 mW/m^2) (Lachenbruch et al., 1985; Bonner et al., 2003; Hauksson, 2011). The highest heat flows in the region take place in the southeastern portion of Salton Sea, including the area where the SSGF is located, owing to the volcanism of Salton Buttes (inverted black triangle in Fig. 6a). I downloaded heat flow values from the SMU Geothermal Lab (http://smu.edu/geothermal/, last accessed in August

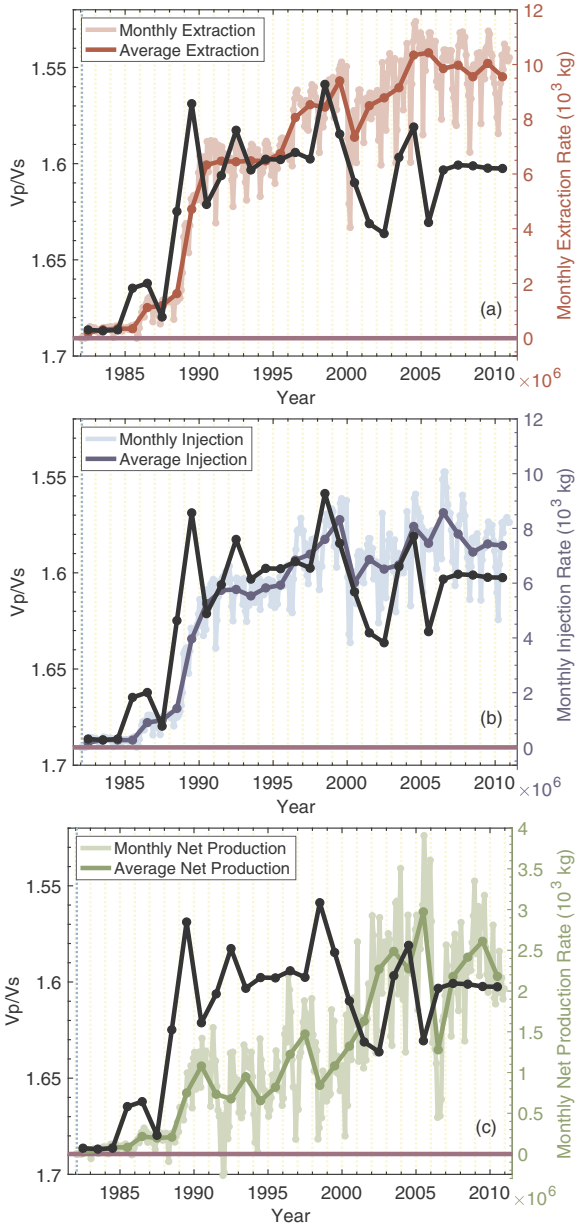

Fig. 7. Temporal variations of the average in situ V_p/V_s ratios (black curve) versus the average operational rate per year of (a) extraction, (b) injection, and (c) net production (i.e. extraction-injection), respectively.

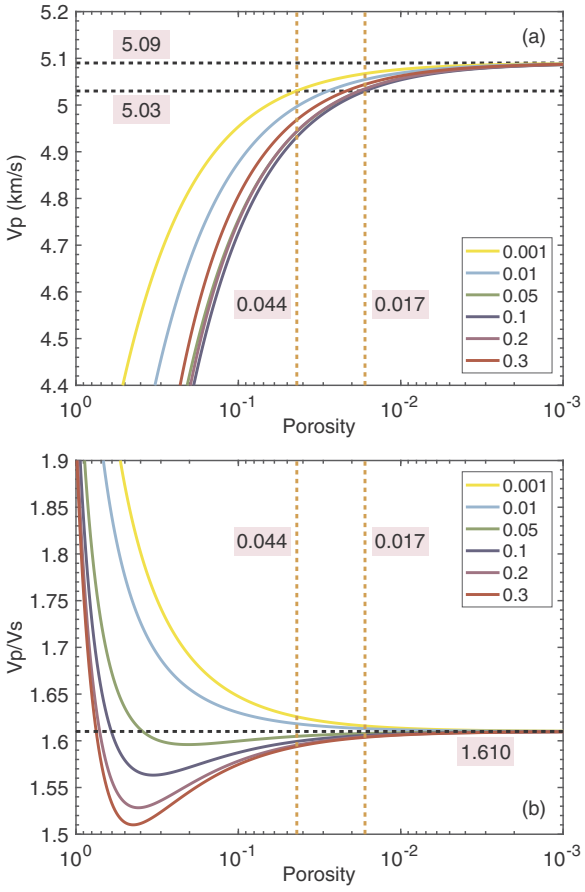

Fig. 8. Velocity variations with water inclusions, as a function of porosity for different aspect ratios according to the theoretical crack model by O'Connell and Budiansky (1974). (a) V_p versus porosity. The horizontal black lines mark the initial and target V_p values for the area. The vertical orange lines set the range of the initial porosity values. (b) V_p/V_s versus porosity. The horizontal line shows the target V_p/V_s ratio of 1.610, which is the average in situ V_p/V_s value of the 6 earthquake clusters. Note that the horizontal axes are reversed in both plots to show decreased porosity.

2018) and plotted them at their site location coordinates in Fig. 6a. These values vary from 150 to 2200 mW/m^2. Depths of most of these measurements are unknown with only one well depth recorded at 3.22 km (boxed triangle in Fig. 6a), close to the average depth of the earthquakes used in the near source V_p/V_s ratio estimation. The resolved in situ V_p/V_s ratios show a general negative correlation with the heat flow values, i.e., low V_p/V_s corresponding to high heat flow. The heat flow values inside the SSGF (enclosed by the pink box) are relatively higher than those outside. The highest heat flow value of 2200 is located near the center of earthquake cluster 1. However, the two wells at the edge of the cluster have relatively lower values of about 375 mW/m^2. Heat flow values are much higher ($>$ 650 mW/m^2) in the central section of the profile where clusters 2, 3, and 4 are located, whereas they are relatively lower ($\sim$ 350 mW/m^2) near cluster 6, which has the highest in situ V_p/V_s ratio. McGuire et al. (2015) also showed that the P velocity variations within the SSGF were correlated with the heat flow patterns up to 30%. The correlations of the newly estimated V_p/V_s values with the tomographic V_p model and heat flow data indicate that the near-source parameters are controlled by natural properties (e.g., mineralogy and temperature) in the subsurface.

6.4. Production data

In order to investigate the effect of the long-term production process on the local V_p/V_s values, I plot the gross injection mass (in kilogram) at the currently active wells in Fig. 6b. The correlation between the estimated V_p/V_s ratios and the injection data is not as clear as with the heat flow data. This is not surprising because the injection amount is constrained by many factors, such as well depths and technical difficulties for drilling. Similar plot is made for the extraction data in Fig. 6c. However, no obvious correlation is observable with the in situ V_p/V_s ratios.

In Fig. 7, I plot the yearly-average V_p/V_s ratios, derived from all the events in the similar clusters, versus the yearly-average monthly rates of the injection, extraction, and net production (i.e. extraction-injection) data from all the wells operated between 1982 and 2010. The extraction and injection operations started in 1982 and the average monthly rates show a general increasing trend over years, although the amount fluctuated from month to month. The average monthly extraction rate remained relatively low through 1985 (Fig. 7a). The V_p/V_s ratio in this period was also stable at about 1.687. As a reference, the V_p/V_s value in

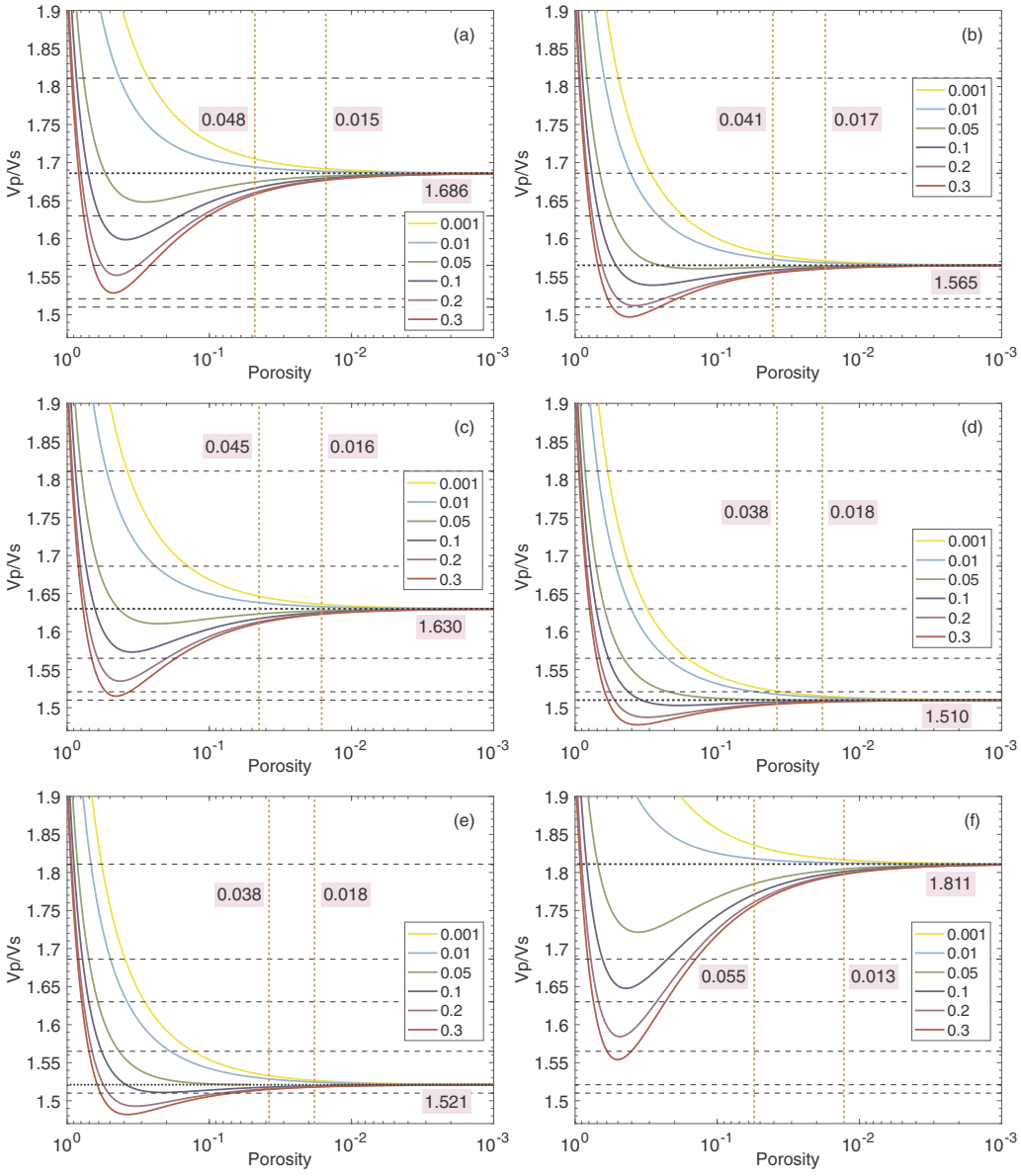

Fig. 9. Similar to Fig. 8, but the target V_p/V_s ratio is the in situ V_p/V_s value for each of the 6 earthquake clusters, respectively. All other symbols are the same as those in Fig. 8.

1981, one year before the geothermal operation started, was also 1.687. The V_p/V_s in 1985 was suddenly reduced to 1.665. Since 1988, all the V_p/V_s ratios in the area are below 1.65 with a few lows and highs. The lowest V_p/V_s ratios of ~1.56–1.58 are observed in 1989, 1998 and 2004, followed by an increase in the next year. After an abrupt increase in 2005, the V_p/V_s ratio was relatively stable until 2010. Although there are lead or lag times throughout the entire time period, the V_p/V_s ratio shows a general negative correlation with the extraction rates, i.e., low V_p/V_s ratio corresponding to high extraction volume. Because the extraction and injection data show similar variation patterns, therefore the net production rates, similar correlations are also observed for the injection and net production data (Fig. 7b and c).

In order to evaluate these correlations quantitatively, I calculate the correlation coefficients between the time series of the in situ V_p/V_s ratio and the production rates. The maximum correlation coefficient is −0.87, −0.87, and −0.80 with zero lag for the extraction, injection and net production data, respectively. In addition, correlation coefficients between all the seismicity rates (shown in Fig. 4) and the production data are also calculated. The maximum coefficient between the seismicity rate for V_p/V_s estimation (orange curve in Fig. 4a) and the production data is 0.64, similar to that in Brodsky and Lajoie (2013) for the same time period. The coefficients of the seismicity rates for the 3 largest clusters with the production data vary from 0.62 to 0.69 and are below 0.3 for the 3 smallest clusters. These calculations imply that the temporal variations in seismicity rates cannot be fully responsible for the observed correlations between the in situ V_p/V_s ratio and the production rates.

6.5. Theoretical crack models

Fig. 7 shows that the extraction and injection activities within the SSGF have altered the local V_p/V_s ratios. In our study time period, the monthly extraction amount has always been greater than the monthly injection (Fig. 7c), except for 5 months in 1980s and early 1990s, resulting in a long-time water depletion in the SSGF. Taira et al. (2018) interpreted their observed long-term velocity increase at shallow depths due to poroelastic contraction that can close cracks and increase seismic velocity. It has been shown that V_p/V_s varies from 1.42 to 1.98 in most

water-saturated rocks (Gregory, 1976). In order to examine whether water inclusions could change the background V_p/V_s ratio to the observed in situ values, I investigate the theoretical crack models discussed in Shearer (1988), which yield similar results at low crack densities and porosities. I present the results from the self-consistent model by O'Connell and Budiansky (1974) because it can explain both the high and low in situ V_p/V_s ratios with water inclusions (Figs. 8 and 9). I require V_p of 1.45 km/s and density of 1.0 g/cm^3 for water-filled cracks and assume ellipsoidal cracks with aspect ratios ranging from 0.001 (very flat) to 0.5 (more spherical).

Because of the long-term water depletion in the study area, I plot V_p and V_p/V_s values in Figs. 8 and 9 as a function of decreased porosity for water-filled cracks with different aspect ratios according to the theoretical crack model. Fig. 8a shows that V_p can increase with decreased porosity to the observed tomographic value of 5.09 km/s. The exception (not shown here) occurs for more spherical cracks (aspect ratios greater than 0.3) with large porosity (close to 1). The long-term velocity increase (~0.04%/year) observed by Taira et al. (2018) was based on seismic recordings from December 2007 to January 2014. If we assume this trend was reliable and the same rate could be applied to our study time period (1982–2010), then the velocity change would be ~1.16%, corresponding to an initial value of 5.03 km/s. According to the theoretical crack model, for cracks with aspect ratios in the range of 0.001–0.3, the porosity values vary from 0.017 to 0.044 at V_p of 5.03 km/s. When cracks close, the porosities are reduced and the V_p can increase to 5.09 km/s. The corresponding V_p/V_s ratios for these cracks would be changed to 1.610 (Fig. 8b), the average value of the in situ V_p/V_s ratios for the 6 similar earthquake clusters. However, whether they increase or decrease to 1.610 depends on their aspect ratios. For flatter cracks (aspect ratio ≤ 0.01), the V_p/V_s ratios will be decreased, whereas they will be increased for more spherical cracks (aspect ratio > 0.01). Similarly, cracks with porosities from 0.013 to 0.055 can have the V_p increased from 5.03 to 5.09 km/s and the V_p/V_s changed to the in situ V_p/V_s ratio for each of the 6 similar earthquake clusters as shown in Fig. 9.

It should be noted that the long-term velocity variation estimated by Taira et al. (2018) was based on a coda window, dominated by scattered surface waves. The same velocity change may not be applied to the body-wave velocity in this study. In addition, the V_p values used in the crack model are the tomographic results, which may not represent near-source values, similar to V_p/V_s. The crack modeling is used to assess the possibility that the observed V_p/V_s ratios could be caused by the anthropogenically induced changes in porosity, but does not explain the exact trend of the temporal variations. A comparison to reservoir monitoring data (e.g., borehole fluid pressure and enthalpy changes) would greatly assist the interpretation of the V_p/V_s changes over time. Unfortunately, no such data are publicly available. More sophisticated models or simulations with the inclusion of monitoring data and information on reservoir geometry and physical properties will be needed to explain the details in the observations.

7. Conclusions

In this study, I apply a high-resolution method to estimate in situ V_p/V_s ratios for 6 similar earthquake clusters in the Salton Sea Geothermal Field. The observed V_p/V_s values are spatially correlated with the tomographic V_p model and the site heat flow data. The calculated yearly average V_p/V_s values show strong negative correlations with the injection and extraction rates. I interpret that the near-source V_p/V_s values are controlled by the subsurface natural properties such as rock composition and geothermal resources, but are affected by the in situ stress change due to the long-term production process. This study also suggests that precisely estimated in situ V_p/V_s ratio can be used to detect near-source changes caused by exploitation of geothermal areas, and is a potentially valuable tool for geothermal resource monitoring.

Acknowledgments

Seismic data used in this study were obtained and originate from the Southern California Earthquake Data Center. Previous velocity model, location catalog and waveform data were collected from published studies listed in the references. I am grateful to the two anonymous reviewers for their constructive and detailed comments. Plots were made using the public domain GMT software and matlab. Funding for this research was provided by the U.S. Geological Survey grant G15AP00116. The Southern California Earthquake Center contribution number for this article is 8919.

References

Barbour, A.J., Evans, E., Hickman, S.H., Eneva, M., 2016a. Sources of subsidence at the Salton Sea Geothermal Field. In: PROCEEDINGS, 41st Workshop on Geothermal Reservoir Engineering Stanford University. Stanford, California, February 22-24, SGP-TR-209. pp. 2016. http://pubs.er.usgs.gov/publication/70168522.

Barbour, A.J., Evans, E.L., Hickman, S.H., Eneva, M., 2016b. Subsidence rates at the southern Salton Sea consistent with reservoir depletion. J. Geophys. Res. 121, 5308–5327. https://doi.org/10.1002/2016JB012903.

Bonner, J.L., Blackwell, D.D., Herrin, E.T., 2003. Thermal constraints on earthquake depths in California. Bull. Seismol. Soc. Am. 93, 2333–2354.

Brodsky, E.E., Lajoie, L.J., 2013. Anthropogenic seismicity rates and operational parameters at the Salton Sea Geothermal Field. Science 341, 543–546. https://doi.org/10.1126/science.1239213.

Chen, X., Shearer, P.M., 2011. Comprehensive analysis of earthquake source spectra and swarms in the Salton Trough, California. J. Geophys. Res. 116, B09309. https://doi.org/10.1029/2011JB008263.

Cheng, Y., Chen, X., 2018. Characteristics of seismicity inside and outside the Salton Sea Geothermal Field. Bull. Seismol. Soc. Am. 108, 1877–1888. https://doi.org/10.1785/0120170311.

Efron, B., Gong, G., 1983. A leisurely look at the bootstrap, the jackknife and cross-validation. Am. Statist. 37, 36–48.

Efron, B., Tibshirani, R., 1991. Statistical data analysis in the computer age. Science 253, 390–395.

Ellsworth, W.L., 2013. Injection-Induced Earthquakes, Science 341, 1225942-1-7. doi: 10.1126/science.1225942.

Foulger, G.R., Grant, C.C., Ross, A., Julian, B.R., 1997. Industrially induced changes in Earth structure at The Geysers geothermal area, California. Geophys. Res. Lett. 24, 135–137.

Gregory, A., 1976. Fluid saturation effects on dynamic elastic properties of sedimentary rocks. Geophysics 41, 895–921. https://doi.org/10.1190/1.1440671.

Gritto, R., Jarpe, S.P., 2014. Temporal variations of Vp/Vs-ratio at The Geysers geothermal field, USA. Geothermics 52, 112–119. https://doi.org/10.1016/j.geothermics.2014.01.012.

Gritto, R., Yoo, S.H., Jarpe, S.P., 2013. Three-dimensional seismic tomography at the Geysers geothermal field, CA, USA. In: Proceedings, Thirty-Eighth Workshop on Geothermal Reservoir Engineering. Stanford University, Stanford, California, February 11-13, 2013, SGP-TR-198.

Hauksson, E., 2011. Crustal geophysics and seismicity in southern California. Geophys. J. Int. 186, 82–98. https://doi.org/10.1111/j.1365-246X.2011.05042.x.

Julian, B.R., Ross, A., Foulger, G.R., Evans, J.R., 1996. Three-dimensional seismic image of a geothermal reservoir: The Geysers, California. Geophys. Res. Lett. 23, 685–688. https://doi.org/10.1029/95GL03321.

Kirkpatrick, A., Peterson, J.J., Majer, E., 1997. Three-dimensional compressional- and shear-wave seismic velocity models for the southeast Geysers geothermal field, California. In: Proceedings 27th Workshop on Geothermal Reservoir Engineering 22 399–410.

Kirschvink, J.L., 1980. The least-squares line and plane and the analysis of palaeomagnetic data, Geophys. J. R. Astron. Soc. 62, 699–718.

Lachenbruch, A., Sass, J., Galanis, S., 1985. Heat-flow in southernmost California and the origin of the Salton Trough. J. Geophys. Res. 90, 6709–6736.

Lees, J.M., Wu, H., 2000. Poisson's ratio and porosity at Coso geothermal area, California. J. Volcanol. Geotherm. Res. 95, 157–173.

Lin, G., 2013. Three-dimensional seismic velocity structure and precise earthquake relocations in the Salton Trough, southern California. Bull. Seismol. Soc. Am. 103, 2694–2708. https://doi.org/10.1785/0120120286.

Lin, G., 2015. Seismic velocity structure and earthquake relocation for the magmatic system beneath Long Valley Caldera, eastern California. J. Volcanol. Geotherm. Res. 296, 19–30.

Lin, G., Amelung, F., Shearer, P.M., Okubo, P.G., 2015. Location and size of the shallow magma reservoir beneath Kīlauea caldera, constraints from near-source Vp/Vs ratios. Geophys. Res. Lett. 42. https://doi.org/10.1002/2015GL065802.

Lin, G., Shearer, P.M., 2007. Estimating local Vp/Vs ratios within similar earthquake clusters. Bull. Seismol. Soc. Am. 97, 379–388.

Lin, G., Shearer, P.M., 2009. Evidence for water-filled cracks in earthquake source regions. Geophys. Res. Lett. 36. https://doi.org/10.1029/2009GL039098.

Lin, G., Thurber, C.H., 2012. Seismic velocity variations along the rupture zone of the 1989 Loma Prieta earthquake, California. J. Geophys. Res. 117. https://doi.org/10.1029/2011JB009122.

Lin, G., Thurber, C.H., Zhang, H., Hauksson, E., Shearer, P.M., Waldhauser, F., Brocher, T.M., Hardebeck, J., 2010. A California statewide three-dimensional seismic velocity model from both absolute and differential times. Bull. Seismol. Soc. Am. 100, 225–240. https://doi.org/10.1785/0120090028.

Lin, G., Wu, B., 2017. Seismic velocity structure and characteristics of induced seismicity at the Geysers Geothermal Field, eastern California. Geothermics 71, 225–233. https://doi.org/10.1016/j.geothermics.2017.10.003.

Llenos, A.L., Michael, A.J., 2016. Characterizing Potentially Induced Earthquake Rate Changes in the Brawley Seismic Zone, Southern California. Bull. Seismol. Soc. Am. 106, 2045–2062. https://doi.org/10.1785/0120150053.

Lohman, R.B., McGuire, J.J., 2007. Earthquake swarms driven by aseismic creep in the Salton Trough, California. J. Geophys. Res. 112. https://doi.org/10.1029/2006JB004596.

McGuire, J.J., Lohman, R.B., Catchings, R.D., Rymer, M.J., Goldman, M.R., 2015. Relationships among seismic velocity, metamorphism, and seismic and aseismic fault slip in the Salton Sea Geothermal Field region. J. Geophys. Res. 120, 2600–2615. https://doi.org/10.1002/2014JB011579.

Michelini, A., Bolt, B.A., 1986. Application of the principal parameters method to the 1983 Coalinga, California, aftershock sequence. Bull. Seismol. Soc. Am. 76, 409–420.

O'Connell, R.J., Budiansky, B., 1974. Seismic velocities in dry and saturated cracked solids. J. Geophys. Res. 79, 5412–5426.

SCEDC, 2013. Southern California Earthquake Center, Caltech. Dataset. doi:10.7909/C3WD3xH1.

Seccia, D., Chiarabba, C., De Gori, P., Bianchi, I., Hill, D.P., 2011. Evidence for the contemporary magmatic system beneath Long Valley Caldera from local earthquake tomography and receiver function analysis. J. Geophys. Res. 116, B12314. https://doi.org/10.1029/2011JB008471.

Shearer, P.M., 1988. Cracked media, Poisson's ratio, and the structure of the upper oceanic crust. Geophys. J. 92, 357–362.

Shearer, P.M., Hardebeck, J.L., Astiz, L., Richards-Dinger, K.B., 2003. Analysis of similar event clusters in aftershocks of the 1994 Northridge, California, earthquake. J. Geophys. Res. 108 (B1), 2035. https://doi.org/10.1029/2001JB000685.

Shearer, P.M., Hauksson, E., Lin, G., 2005. Southern California hypocenter relocation with waveform cross-correlation, Part 2: results using source-specific station terms and cluster analysis. Bull. Seismol. Soc. Am. 95, 904–915.

Taira, T., Nayak, A., Brenguier, F., Manga, M., 2018. Monitoring reservoir response to earthquakes and fluid extraction, Salton Sea geothermal field, California. Sci. Adv. 4. http://advances.sciencemag.org/content/4/1/e1701536.abstract.

Takei, Y., 2002. Effect of pore geometry on Vp/Vs: From equilibrium geometry to crack. J. Geophys. Res. 107. https://doi.org/10.1029/2001JB000522.

Walck, M.C., 1988. Three-dimensional Vp/Vs variations for the Coso Region, California. J. Geophys. Res. 93, 2047–2052. https://doi.org/10.1029/JB093iB03p02047.

Zhang, Q., Lin, G., 2014. Three-dimensional Vp and Vp/Vs models in the Coso geothermal area, California: Seismic characterization of the magmatic system. J. Geophys. Res. 119, 4907–4922. https://doi.org/10.1002/2014JB010992.

Zhang, Q., Lin, G., Zhan, Z., Chen, X., Qin, Y., Wdowinski, S., 2017. Absence of remote earthquake triggering within the Coso and Salton Sea geothermal production fields. Geophys. Res. Lett. https://doi.org/10.1002/2016GL071964.